Journal of Power Sources 196 (2011) 5503–5510

Contents lists available at ScienceDirect

Journal of Power Sources

journal homepage: www.elsevier.com/locate/jpowsour

The effect of temperature on corrosion behavior of SS316L in the cathode environment of proton exchange membrane fuel cells

Ying Yang [a], Liejin Guo [a,**], Hongtan Liu [a,b,*]

[a] State Key Laboratory of Multiphase Flow in Power Engineering, Xi'an Jiaotong University, Xi'an, Shaanxi 710049, PR China
[b] Department of Mechanical and Aerospace Engineering, University of Miami, Coral Gables, FL 33124, USA

ARTICLE INFO

Article history:
Received 7 January 2011
Received in revised form 18 February 2011
Accepted 21 February 2011
Available online 26 February 2011

Keywords:
Bipolar plate
Corrosion
Proton exchange membrane fuel cell (PEMFC)
Stainless steel
Passive film
Photo-electrochemistry (PEC)

ABSTRACT

The effect of temperature on the corrosion behavior of SS316L in simulated proton exchange membrane fuel cell (PEMFC) environments has been systematically studied. Electrochemical methods, both potentiodynamic and potentiostatic, are employed to characterize the corrosion behavior. Atomic force microscope (AFM) is used to examine the surface morphology and X-ray photoelectron spectroscopy (XPS) analysis is used to identify the composition and the depth profile of the passive film. Photo-electrochemical (PEC) measurements are also performed to determinate the band gap energy of the passive film semiconductor. Interfacial contact resistances (ICR) between polarized SS316L and carbon paper are also measured. The experimental results show that corrosion resistance decreases with temperatures even though the thickness of passive film increases with temperature, at a given cell potential, the corrosion behavior of SS316L can be significantly different at different temperatures in PEMFC cathode environments, and the band gap of passive films decrease with temperature. The results also show that within the temperature range studied (25–90 °C), after different passivation time, the corrosion current densities of SS316L are all lower than the US DOE 2015 target value of 1 $\mu A\,cm^{-2}$, but the ICR between the carbon paper and polarized SS316L does not satisfy the US DOE 2015 target.

1. Introduction

The voltage of a single cell in a proton exchange membrane fuel cell (PEMFC) is very low, around 0.5–0.8 V when drawing a useful current. Thus many single cells are connected in series to form a stack via bipolar plates. A bipolar plate connects the surface of the anode of one cell and the cathode of next cell. At the same time, it feeds the hydrogen gas and air through the flow channels to the electrodes and provides structural support for gas diffusion layer (GDL)/membrane electrode assembly (MEA). Because bipolar plates are in contact with the GDL/MEA, their materials must have high electrical conductivity and good corrosion resistance [1,2]. High electrical conductivity minimizes electrical losses and good corrosion resistance prevent dissolved metal ions to pollute proton exchange membrane and decreasing the cell efficiency. Stainless steels have good conductivity, good mechanical strength and low cost for shaping, thus they are good candidates for bipolar plates. Austenite stainless steels have been studied as bipolar plate materials for PEMFC in [3–10].

A PEMFC has a typical working temperature from room temperature to about 100 °C [11–17]. When a PEMFC stack operate at an efficiency of about 50%, the remaining 50% of the chemical energy is converted into waste heat [15]. Removing waste heat effectively from a fuel cell stack, or thermal management, is a critical issue in fuel cell power systems. Sometimes, coolant (e.g. water) flowing in internal coolant channels in bipolar plates is use to remove the waste heat to maintain proper operating temperature [2,16]. However, current distribution [14], relative humidity [17], reactant gas partial pressure [17], reactant gas flow rate [15] and working time [14,15,17] can influence the temperature distribution in PEMFC stacks. Wilkinson et al. [14] found that the temperature of bipolar plate changed from 30 °C to 60 °C with current density variation from 0.1 $A\,cm^{-2}$ to 1 $A\,cm^{-2}$, and the difference of temperature between gas inlet and outlet was about 5 °C when fuel cell was running at 1 $A\,cm^{-2}$. Fabian et al. [17] studied the spatial and temporal distributions of temperature in the mass transport layer immediately above the planar, horizontal cathode of PEMFC driven by natural convection. They reported that the temperature of fuel cell increased about 20 °C during a standard polarization scan. Wen and Huang [15] operated a PEMFC in a constant voltage discharge mode at different oxygen flow rates and concluded that there were temperature differences of 10–15 °C along the channel. According

* Corresponding author at: Department of Mechanical and Aerospace Engineering, University of Miami, Coral Gables, FL 33124, USA. Tel.: +1 305 284 2019; fax: +1 305 284 2580.
** Corresponding author at: Xi'an Jiaotong University, Xi'an, Shaanxi 710049, PR China. Tel.: +86 29 82663895; fax: +86 29 8266 9033.
E-mail addresses: youngying@gmail.com (Y. Yang), lj-guo@mail.xjtu.edu.cn (L. Guo), hongtanliu@mail.xjtu.edu.cn, hliu@miami.edu (H. Liu).

0378-7753/$ – see front matter © 2011 Elsevier B.V. All rights reserved.
doi:10.1016/j.jpowsour.2011.02.070

to the studies mentioned above, it is clear that temperature distribution in a PEMFC or a fuel cell stack is not uniform. Therefore, it is important to study corrosion behavior of bipolar plate materials under different temperatures.

Nikam and Reddy [18] studied the corrosion behavior of copper–beryllium alloy (type: C-17200) in solution of 5% (v/v) HCl + 5% (v/v) Na_2SO_4. They found the corrosion currents (at the free corrosion potential) of C-17200 increased with increasing temperature under non-oxidizing conditions. Nikam et al. [6] studied the corrosion resistance of low temperature carburized (LTC) SS316 in solution of 0.5 M H_2SO_4 (pH 4.0) at 25 °C and 80 °C, respectively. They pointed out that the corrosion potential of LTC SS316 at 80 °C decreased about 0.1 V with respect to LTC SS316 at 25 °C, and corrosion current (at free corrosion potential) increased about one order of magnitude. Wang and Northwood [10] studied the corrosion performance of SS316L in 0.5 M H_2SO_4 solution at 20 °C and 70 °C, respectively. They reported that the corrosion current (at the free corrosion potential) of SS316L is 40.3 $\mu A\,cm^{-2}$ at 70 °C and 4.9 $\mu A\,cm^{-2}$ at 20 °C; the corrosion potential of SS316L at 70 °C is slightly lower than that at 20 °C. Jin et al. [19] studied the corrosion behavior of amorphous alloy $Zr_{75}Ti_{25}$ and SS316L at 25 °C and 80 °C, respectively. They found that the corrosion rates of both materials in simulated PEMFC environment at 80 °C are higher than that at 25 °C. El-Khatib et al. [20] studied the corrosion performance of SS316L at 25 °C and 80 °C, respectively and found that the passivation current of SS316L in simulated PEMFC environment at 80 °C increases about one order of magnitude in contrast to that at 25 °C. García and Smit [21] deposited polypyrrole (PPy) film on SS304 (PPy/SS304) and found the corrosion current (at the free corrosion potential) of PPy/SS304 decreases two orders of magnitude with respect to naked SS304 at room temperature and four orders of magnitude at 60 °C. Besides, Pozio et al. [7] and Silva et al. [22] applied varying temperature condition to simulate PEMFC environment temperature, they increase the temperature from 25 °C to 70 °C in working days and decrease to 25 °C in the weekends.

It is obvious that most of the above studies focused on the comparisons of the material performance at room temperature and a specific working temperature, but the bipolar plate material could experience a wide range of temperatures in a fuel cell depending on the locations and time. Besides, some studies [6,10,18,21] only compared the corrosion current at the free corrosion potential, but information about corrosion current at PEMFC working potentials are very valuable. It is important to understand the corrosion behavior of bipolar plate materials under different temperatures in order to develop appropriate surface treatments and to provide guidelines for bipolar plate structure optimizations. Therefore, it is the main objective of this study to systematically study the effect of temperature on the corrosion behavior of SS316L, a very popular candidate for bipolar plate material in PEMFCs.

2. Experimental

2.1. Simulated solutions and specimens

2.1.1. Simulated solutions

Following the study by Agneaux et al. [4] and previous work [23,24], a solution of 1×10^{-5} M H_2SO_4 with 6×10^{-4} M F^- was chosen as the simulated solution for the PEMFC cathode corrosion environment in this study. The pre-bubbling air was carried out about 1 h before each measurement and the solution was bubbled with air during measurement. The temperatures of solution were controlled at 25 °C, 50 °C, 70 °C and 90 °C, respectively.

2.1.2. Specimens

The stainless steel is purchased from a commercial company. The main chemical compositions of SS316L are analyzed by S4 PIONEER X-ray fluorescence spectrometry (BRUKER, Germany) and are shown in Table 1.

Table 1
Main chemical composition of SS316L (wt.%).

C	Cr	Ni	Mo	Si	Cu	Fe
0.03	16.9	10.5	2.23	0.516	0.506	Balance

SS316L specimens were machined into cylinders with a diameter of 10 mm and a length of 7 mm. One end and the side of the specimens were sealed by silicone and polyethylene heat-shrink tube, leaving only one end exposed. The sealed end of the specimen was connected with a copper wire and the exposed end was used as the working surface for electrochemical measurement. The working surface was polished with 800-grit silicon carbide abrasive paper, rinsed with acetone and de-ionized water, and dried in nitrogen gas.

2.2. Electrochemistry

2.2.1. Corrosion cell and reference electrode

The electrochemical experiments were carried out in a corrosion cell consisting of a three-electrode arrangement, one gas inlet tube and one gas outlet tube. The specimen served as the working electrode and a platinum sheet as the counter electrode.

Because there is a significant variation in potential with temperature for saturated calomel electrode (SCE), around $-0.67\,mV\,K^{-1}$ [25] and SCE is not suitable for above 70 °C [26], a calomel electrode with 0.1 M KCl ($CE_{0.1\,M\,KCl}$) is used as the reference electrode in this study. The potential at 25 °C and temperature coefficient of $CE_{0.1\,M\,KCl}$ are 0.336 V vs. the normal hydrogen electrode (NHE) and $-0.08\,mV\,K^{-1}$, respectively [27]. Thus the potential variation of $CE_{0.1\,M\,KCl}$ can be neglected from 25 °C to 90 °C. The $CE_{0.1\,M\,KCl}$ connects to a salt-bridge probe filled with 0.1 M KCl and equipped with a Vycor frit tip. All the potentials are referred to the $CE_{0.1\,M\,KCl}$ except specified otherwise.

The corrosion cell was immersed in a temperature-controlled water bath. The tests were conducted using a PAR 273A potentiostat (EG&G) coupled with a 5210 lock-in Amplifier (Signal recovery). PowerSuite software was used for electrochemical data acquisition and processing. Each experiment was repeated by using three different specimens to confirm reproducibility of the results.

2.2.2. Electrochemical measurements

At the beginning of each experiment, the specimen was polarized cathodically for 10 min to remove oxide on the specimen surface. In potentiodynamic tests, specimens were stabilized at open circuit potential (OCP) for 1 h after cathodic polarization, then were polarized at a scanning rate of $1\,mV\,s^{-1}$ in a potential range from −0.2 V vs. OCP to 1.1 V vs. $CE_{0.1\,M\,KCl}$ (1.436 V vs. NHE). In potentiostatic test, specimens were held at a potential of 0.5 V (0.836 V vs. NHE) to simulate PEMFC cathode condition. After polarizing cathodically for 10 min the specimen was potentiostatic polarized for 5 h.

In Mott–Schottky measurements, potential sweeps were carried out from anodic potential 0.3 V to cathodic potential of −0.3 V at a scan rate of 50 mV per step. The acquisition frequency was 188 Hz.

2.3. Photo-electrochemistry

Photo-electrochemical (PEC) experiments were carried out in a PEC cell equipped with a flat quartz optical window. The test cell was kept at a given temperature with a water jacket and was bubbled thoroughly with pressurized air prior to and during the PEC measurements. PEC measurements also used the three-electrode arrangement. The specimen polarized at 0.5 V for 5 h in a solu-

tion 1×10^{-5} M H_2SO_4 with 6×10^{-4} M F^- at different temperature served as the working electrode and the PEC experiments were performed in the same solution, a platinum sheet as the counter electrode and a $CE_{0.1\,M\,KCl}$ as the reference electrode.

The photocurrents were generated by illuminating the entire working electrode surface by a 500 W Xenon lamp and a 1200 mm^{-1} grating monochromator. A PAR 273A potentiostat (EG&G) coupled with a 5210 lock-in Amplifier (Signal recovery) and a light chopper (PAR 197, EG&G, f = 17.3 Hz) were used to measure the photocurrent, and the PEC system was controlled by a software developed in-house. The photocurrent spectra were obtained on specimens polarized at 0.5 V by scanning the wavelength of light in steps of 10 nm from 320 nm to 650 nm. The photocurrent was corrected for the output of the lamp and the efficiency of the monochromator by using a calibrated photodiode. Calibration was performed before and after every set of experiment.

2.4. Surface morphology

Atomic force microscope (AFM) was used to characterize the surface morphology of specimens potentiostatic polarized at different temperatures. The measurements were carried out by Solver Next type AFM (NT-MDT). In the measurements, the semi-contact mode was used, scan rate was 2 Hz and scan area was 1 μm × 1 μm. Surface morphology and roughness were analyzed by "Image Analysis" software (NT-MDT, version 3.5.0.1016).

2.5. Composition of passive films

To identify the composition and the depth profile of passive film on the specimen surface, X-ray photoelectron spectroscopy (XPS) was taken after the specimen was potentiostatic polarized at 0.5 V for 5 h in 1×10^{-5} M H_2SO_4 with 6×10^{-4} M F^- solution. The composition profiles of the elements Fe 2p, Ni 2p, Cr 2p and O 1s in the passive film were analyzed, and was carried out with an AXIS Ultra^{DLD} X-ray photoelectron spectroscope (Kratos Analytical) using a monochromatic Al Kα radiation X-ray source (1486.6 eV). Binding energies were referenced to the C 1s peak at 285.1 eV. The chamber base pressure was 1.7×10^{-9} Torr (2.266×10^{-7} Pa). Sputtering was performed at a pressure of about 1.7×10^{-6} Torr (2.266×10^{-4} Pa) with 3.0 keV argon ions beam, while the sputtered area was 2 mm × 2 mm. The sputtering rate was determined to be around 3.3 nm min^{-1}. The data processing of the different peaks were calculated by the "Vision Processing" software (Kratos Analytical).

2.6. Interfacial contact resistance (ICR)

In order to examine the conductive property of SS316L in PEMFC cathode environments, the interfacial contact resistance (ICR) between the specimen surface and carbon paper were measured. A carbon paper was sandwiched between the specimen surface and a gold coated copper plate. An electrical current of 2.5 A was provided by a constant current source through the specimen and the gold coated copper plate. The compression force was applied by means of a manual HV-500II test stand (IMADA) and the force was monitored with a Z2-500N digital force gauge (IMADA). The compression force was applied on the specimen gradually, and the total voltage was measured through a FLUKE 17B digital Multimeter. The schematic of the assembly for ICR measurement and the detailed experimental descriptions are given in [24].

Before ICR measurements, specimens were polarized potentiostatically at 0.5 V at different temperature for 5 h, then cleaned with de-ionized water and dried in the air. In order to ensure the reliability of the ICR measurement results, each measurement is repeated three time with three different specimens polarized under the same condition and the averaged value for each temperature is presented.

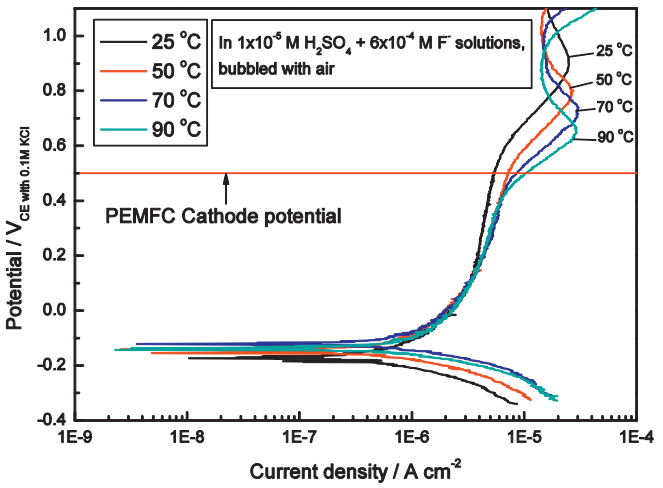

Fig. 1. Polarization curves for SS316L at different temperatures (25 °C, 50 °C, 70 °C and 90 °C) in 1×10^{-5} M H_2SO_4 + 6×10^{-4} M F^- solutions bubbled with air.

3. Results and discussion

3.1. Potentiodynamic study

Fig. 1 shows potentiodynamic polarization curves for SS316L at different temperatures in the simulated solutions bubbled with air. The polarization curves show the existence of the self-passivation behavior for SS316L at all temperatures. The results show that, as the temperature increases, the passive region becomes narrower and the pitting potential decreases, indicating that the corrosion resistance decreases with increasing temperature. Carranza and Alvarez [28] also observed a similar phenomena for Fe–Cr–Ni alloys in 0.1 M Na_2SO_4 solution, where the pitting potential decreasing with the increase of temperature. When polarization potentials are higher than 0.5 V, a anodic peak appears, due to transpassivation, probably resulting from the valence change of chromium from lower valence to higher valence [28–30]. Besides, the position of peaks decreases with the increase of temperature, indicating that the transpassvation dissolution starts at lower potential and becomes more severe at higher temperatures.

For SS316L, the typical PEMFC cathode working potential (0.5 V) lies in the passivation region at 25 °C, in the pitting potential at 50 °C, and in transpassivation region at 70 °C and 90 °C. Hence, corrosion behavior of SS316L is significantly different at different temperatures in PEMFC cathode environments. Consequently, to avoid excessive corrosion of SS316L bipolar plates in PEMFC cathode, operating potential should be taken into consideration when deciding on the operating temperature.

3.2. Potentiostatic study

Potentiostatic measurements were performed for 5 h to study the long-term corrosion resistance of SS316L in 1×10^{-5} M H_2SO_4 + 6×10^{-4} M F^- solutions with different temperatures and the results are shown in Fig. 2.

When SS316L is applied with a constant potential of 0.5 V, there is a fast decay for the current density of SS316L at every temperature, due to the rapid passivation of the fresh surface of specimens in cathodic environment. The currents are stabilized after about 1500 s for 25 °C and 50 °C, indicating that a stable passive state is established; after 2000 s, the corrosion current densities are lower than US DOE 2015 target, 1 μA cm^{-2} [31]. The currents of SS316L

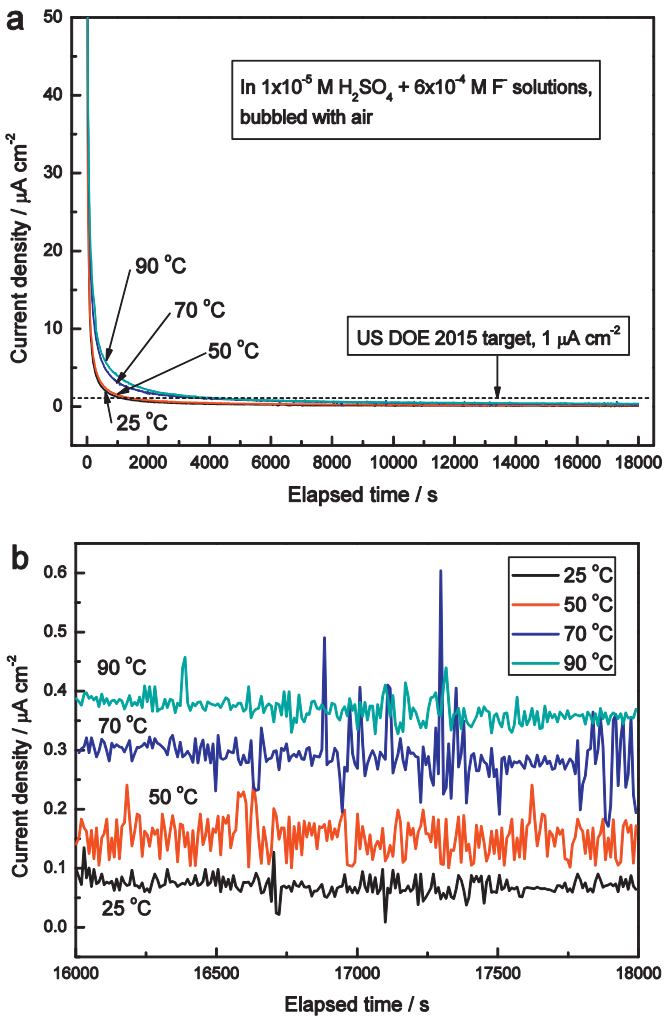

Fig. 2. Potentiostatic plots (a) and the current densities from 16,000 s to 18,000 s (b) for SS316L at different temperatures (25 °C, 50 °C, 70 °C and 90 °C) in 1×10^{-5} M $H_2SO_4 + 6 \times 10^{-4}$ M F^- solutions bubbled with air.

are stabilized after about 2000–3000 s at 70 °C and 90 °C, indicating that the passivation of SS316L surface is slower at relative high temperatures; besides, the corrosion current densities are lower than US DOE 2015 target only after about 4000 s. From Fig. 2(b), the result shows that the higher the temperature is, the higher are the corrosion current densities. This trend is similar to what was found in the potentiodynamic studies. It can also be seen that current density decreases continuously with continued potentiostatic polarization.

3.3. Surface morphology

The surface morphology of SS316L potentiostatic polarized at different temperature is examined by atomic force microscope (AFM) and the results are shown in Fig. 3. Note that the overall ridges and valleys are caused by the polishing of the specimens. It is clearly seen that the size and height of the peaks increases with increase of temperature. The results of root-mean-square (RMS) roughness analyses show that the RMS roughness is 2.79 nm at 25 °C, 3.98 nm at 50 °C, 4.30 nm at 70 °C and 8.17 nm at 90 °C, respectively. Clearly, the AFM results show that the roughness of SS316L increases significantly with increasing temperature, indicating that the corrosion activity increases with increasing temperature, which confirms the results of the potentiostatic studies (Fig. 2).

3.4. Mott–Schottky analyses

The semiconductor behavior of passive films at the interface of passive film-electrolyte can be determined by Mott–Schottky method. The potential dependence of space charge layer at a passive film-electrolyte interface is described by the Mott–Schottky equation [32]:

$$\frac{1}{C^2} = \frac{2}{eN_D\varepsilon\varepsilon_0}\left(E - E_{fb} - \frac{kT}{e}\right) \quad (1)$$

for an n-type semiconductor and

$$\frac{1}{C^2} = \frac{2}{-eN_A\varepsilon\varepsilon_0}\left(E - E_{fb} - \frac{kT}{e}\right) \quad (2)$$

for a p-type semiconductor, where C is the capacitance of the space charge layer; ε the dielectric constant of the film; ε_0 the permittivity of free space; e the electron charge; N_D and N_A the donor and acceptor densities, respectively; E the applied potential; E_{fb} the flat band potential; k the Boltzmann's constant; and T the absolute temperature. The validity of the Mott–Schottky analysis is discussed in [33].

Fig. 4 shows the Mott–Schottky plots of SS316L polarized at 0.5 V for 5 h at different temperatures in a solution of 1×10^{-5} M $H_2SO_4 + 6 \times 10^{-4}$ M F^- bubbled with air. The Mott–Schottky results show that the passive films formed at different temperatures are of a bi-layer (p–n type) semiconductor, but the p-type semiconductor behavior becomes weaker with the increase of temperature and at 90 °C, the bi-layer structure disappears. The passive film behaves as an n-type semiconductor when the applied potential is in the range from 0.3 V to about −0.15 V and a p-type semiconductor when the applied potential is in the range from about −0.15 V to −0.3 V. The Mott–Schottky results show that the passive films behave more as an n-type semiconductor, and the structure facilitates the growth of passive films due to its promotion of metal ions to migrate from the substrate to the films, however the structure cannot completely prevent harmful ions (such as F^- and SO_4^{2-}) from penetrating the metal substrate leading to local corrosion, as reported in previous studies [23,24]. It can be observed that the flat band potential (the turning point of n-type behavior to p-type behavior [34]) for SS316L decreases with the increase of temperature (even though the difference between maximum and minimum is only 0.05 V), the band bending of n-type semiconductor increases with the increase of temperature.

3.5. Composition of passive films

The composition profiles of elements Fe 2p, Cr 2p, Ni 2p and O 1s in the passive films formed on SS316L polarized at 0.5 V in a 1×10^{-5} M $H_2SO_4 + 6 \times 10^{-4}$ M F^- solution for 5 h at different temperatures, were obtained by X-ray photoelectron spectroscopy (XPS). The results are showed in Fig. 5. The depth profiles of Cr/Fe atomic ratio for the passive films are showed in Fig. 6.

The thickness of passive film was obtained from the surface to the profile with highest peak of Cr^{3+}. Using this method, it is found that the thickness of the passive film formed on SS316L with increasing temperature is 5.1 nm (at 77 s), 5.2 nm (at 80 s), 5.5 nm (at 100 s) and 6.6 nm (at 120 s), respectively. Hence, the thickness of passive film increases with the increase of temperature. According to semiconductor energy band theory, when an n-type semiconductor was applied the same potential (higher than flat band potential), the flat band potential of semiconductor is lower, the band bending is stronger, so that the transfer of metal anions and oxygen vacancies from the metal substrate to the film/electrolyte interface is enhanced, i.e., the film becomes thicker [35], which is in agreement with the results of XPS studies presented above.

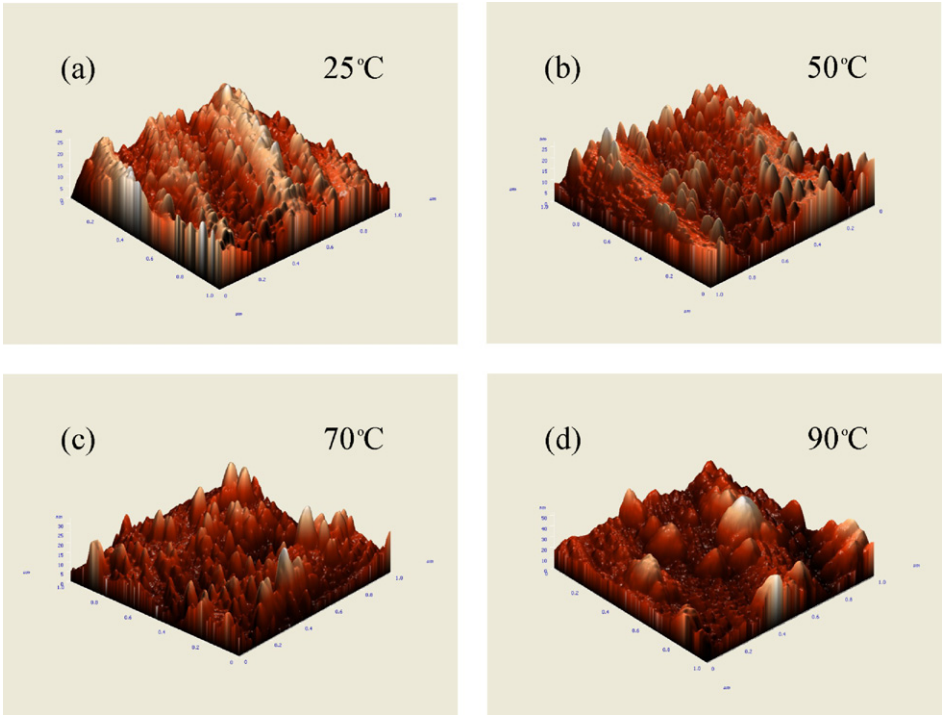

Fig. 3. Surface morphology of SS316L polarized in 1×10^{-5} M $H_2SO_4 + 6 \times 10^{-4}$ M F^- solution at different temperatures. (a) 25 °C, (b) 50 °C, (c) 70 °C and (d) 90 °C.

From Fig. 5, it is found that the content profile of Cr can be divided into three regions in the depth profile. In the first region, from the surface to 5–6 nm, Cr content increases and reaches a maximum; in the second region, from 5–6 nm to about 19 nm from the surface, it decreases from the maximum value to the value in the substrate; in the third region, greater than 19 nm, the Cr content is constant, i.e., it remains the same as in the original substrate. In the first region, Fe content increases sharply first then changes slightly; in the second region, Fe content gradually increases to the content in the substrate. In this study, thickness of the passive film corresponds to the depth of the first region. From Fig. 6, it is clear that within the passive film thickness, the Cr/Fe atomic ratio decreases to a minimum within a very thin layer and then increases to a maximum rapidly. According to the above observations, the passive film can be considered to be consisting of two layers, an outer layer and an inner layer. The XPS results also show that the relative content of Cr in the passive film decreases with the increase of temperature, which indicates that the relative content of Cr in passive films decreases with the increase of temperature. The decrease of relative content of Cr oxide in passive films leads to the decrease of corrosion resistance of SS316L. Therefore, it is believe that the difference of relative dissolution rates of Cr and Fe results in the semiconductor structure change of the passive film at different temperature, hence leads to the difference of corrosion resistance of stainless steel under long-term running condition.

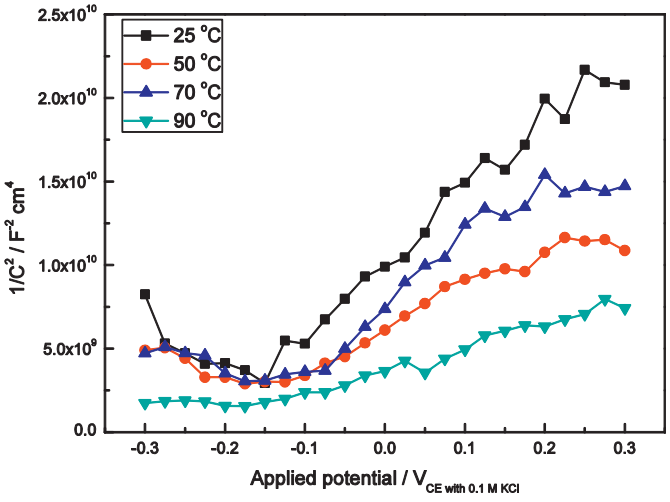

Fig. 4. Mott–Schottky plots for SS316L at different temperature (25 °C, 50 °C, 70 °C and 90 °C) in 1×10^{-5} M $H_2SO_4 + 6 \times 10^{-4}$ M F^- solutions bubbled with air.

3.6. Photo-electrochemical analyses

There is a simplified relationship between photocurrent and photon energy of the incident light for passive films [36],

$$\frac{i_{ph}h\nu}{I} = \alpha(h\nu - E_g)^2 \quad (3)$$

where i_{ph} is photocurrent, $h\nu$ the photon energy of the incident light, I the intensity of incident light, α optical absorption coefficient and E_g the band gap energy. The band gap can be obtained by extrapolating the $(i_{ph}h\nu/I)^{0.5}$ plots from the corresponding photocurrent spectra, and the intercept of the straight line with the photon energy axis is the band gap of the semiconductor.

Fig. 7(a) shows $(i_{ph}h\nu/I)^{0.5}$ vs. $h\nu$ plots and the band gap energy can be estimated as the photon energy at which $(i_{ph}h\nu/I)^{0.5}$ equals to zero. Fig. 8 shows the band gap energies of the passive film formed at different temperatures (25 °C, 50 °C, 70 °C and 90 °C) are 2.82 eV, 2.79 eV, 2.62 eV and 2.59 eV, respectively. From Fig. 8, it can be seen that the band gap becomes narrower as temperature increases. Thus, it is easier to generate photocurrent for passive films formed on SS316L at higher temperature. Fig. 7(b) shows that photocurrents are positive during illumination, indicating that the passive film behaves more as a n-type semiconductor.

The XPS and Mott–Schottky analysis results indicate the passive films formed in PEMFC cathode environments are mainly composed of Fe oxide (Fe_2O_3 primarily) and Cr oxide (Cr_2O_3 primarily). The

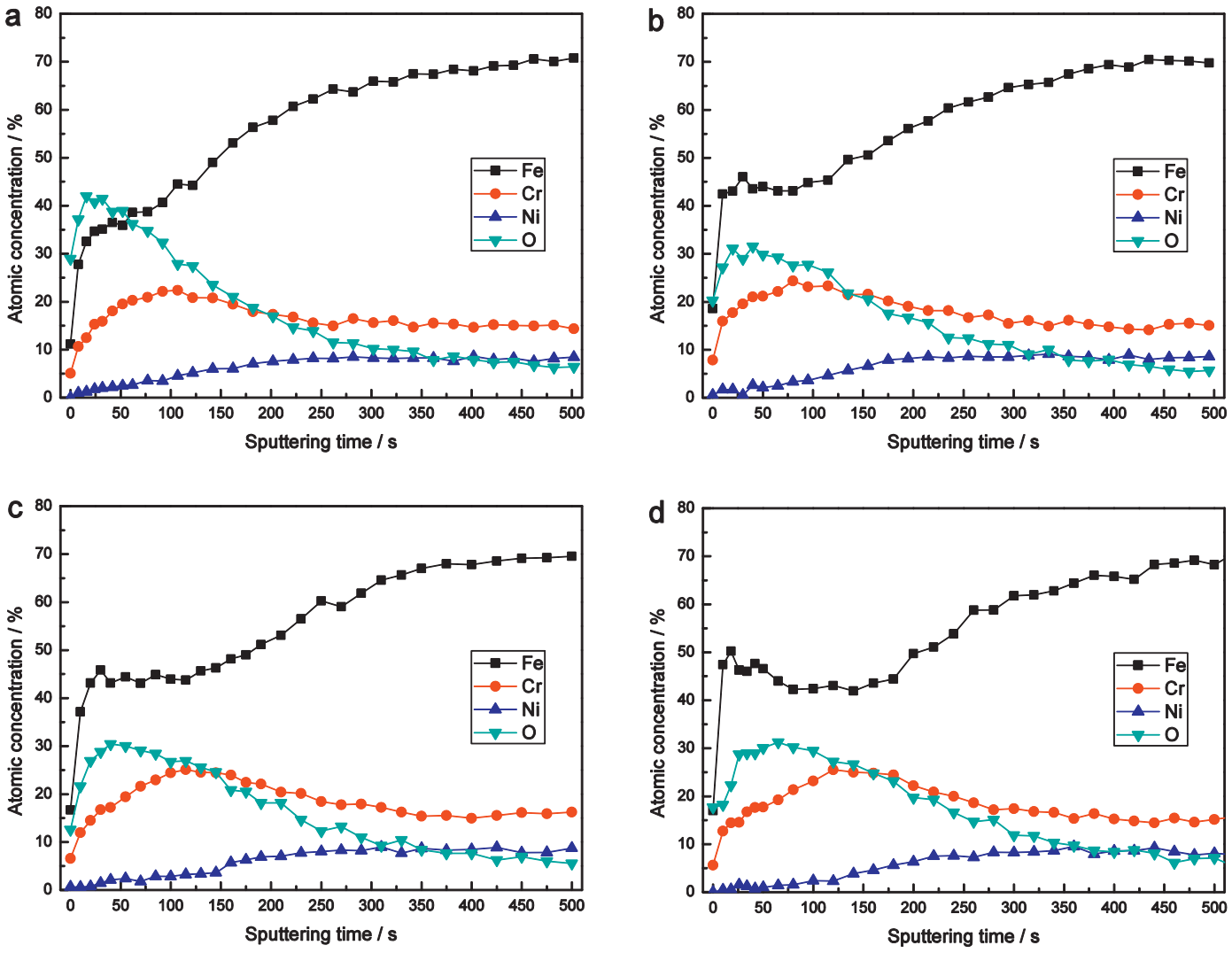

Fig. 5. XPS depth profiles of passive films formed on SS316L polarized at 0.5 V in 1×10^{-5} M $H_2SO_4 + 6 \times 10^{-4}$ M F^- solutions for 5 h at different temperatures. (a) 25 °C, (b) 50 °C, (c) 70 °C and (d) 90 °C.

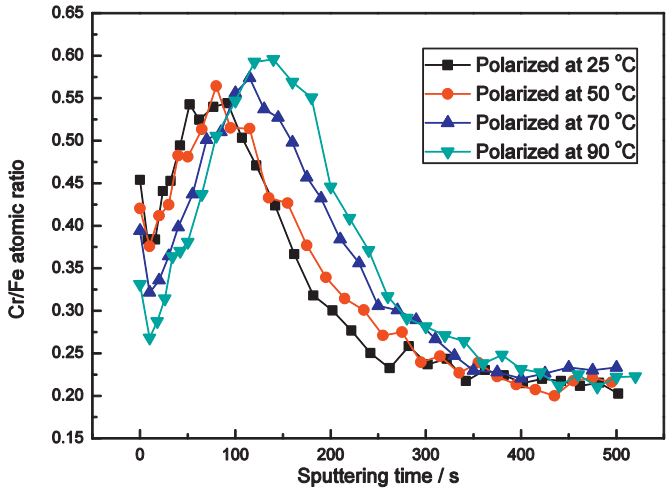

Fig. 6. Cr/Fe atomic ratio for the passive film formed on SS316L polarized at 00.5 V in 1×10^{-5} M $H_2SO_4 + 6 \times 10^{-4}$ M F^- solutions for 5 h at different temperatures (25 °C, 50 °C, 70 °C and 90 °C).

band gap of Cr_2O_3 is in the range of 2.7–2.9 eV [37] and that of Fe_2O_3 is in the range of 1.85–2 eV [38]. The PEC measurement results show that the band gap of passive films formed in PEMFC cathode environments lies between them. The passive film can be considered to contain Cr_2O_3 doped with Fe_2O_3 and the content of Fe_2O_3 increase with the increase of temperature, as shown in Fig. 6. Thus the band gap of the passive film decreases toward the value for Fe_2O_3 as the temperature increases.

3.7. Interfacial contact resistance

Fig. 9 displays the results of ICR between the carbon paper and SS316L polarized at 0.5 V for 5 h at different temperatures in 1×10^{-5} M $H_2SO_4 + 6 \times 10^{-4}$ M F^- solutions bubbled with air. All the specimens exhibited higher ICR than that of original specimens. The ICR values under 140 N cm^{-2} for the original specimen is 20.5 mOhm cm^2, three times greater than the US DOE 2015 target value of 5 mOhm cm^2 at 140 N cm^{-2} (10 mOhm cm^2 for both sides of one plate) [31]. It can also be seen from Fig. 9 that the ICR increases with increasing the environment temperature. Since the ICR of SS316L polarized in PEMFC cathode environments cannot satisfy the US DOE 2015 target, improving the surface conductivity of SS316L is very important for its application in PEMFCs.

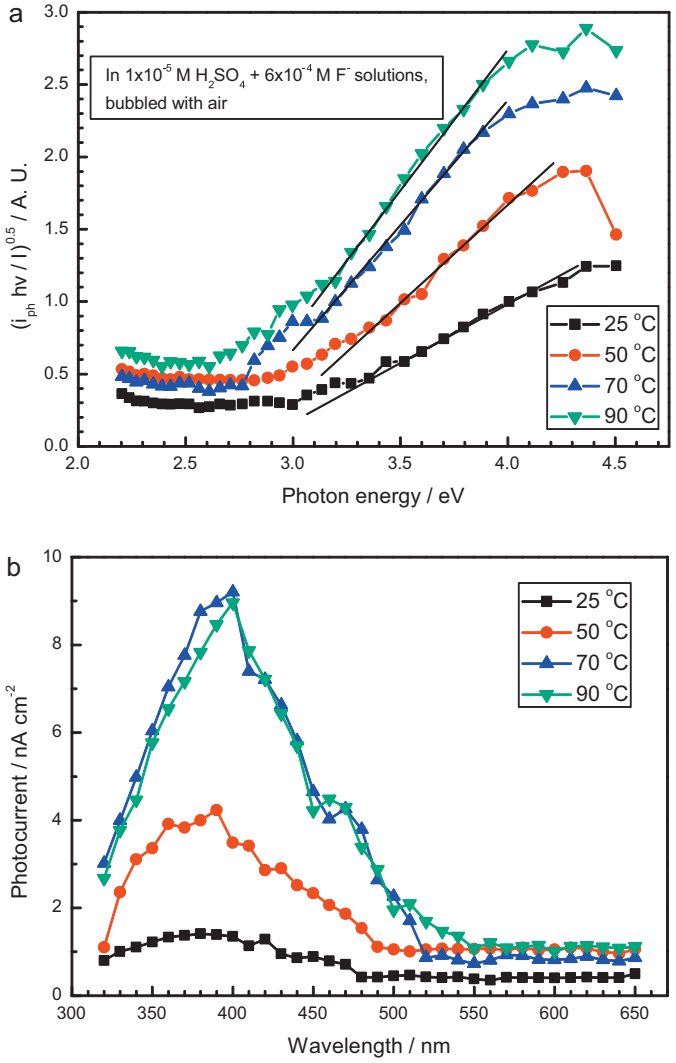

Fig. 7. (a) $(i_{ph}h\nu/I)^{0.5}$ vs. $h\nu$ plots for SS316L polarized at 0.5 V for 5 h at different temperatures in 1×10^{-5} M $H_2SO_4 + 6 \times 10^{-4}$ M F^- solutions. (b) Raw photocurrent spectrum data.

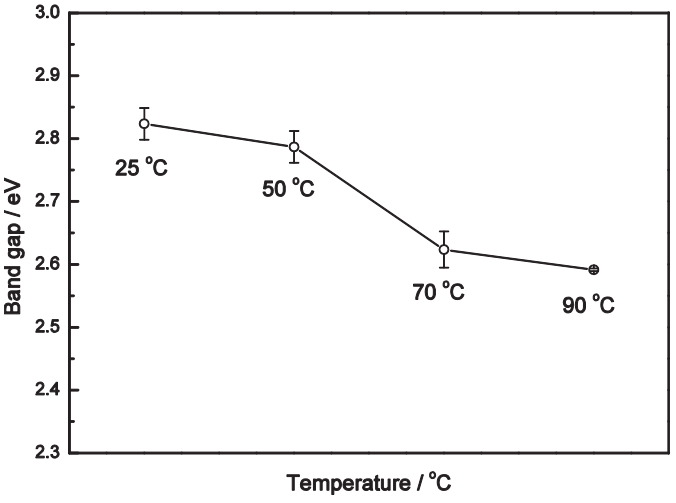

Fig. 8. Band gap of passive film formed on SS316L polarized at 0.5 V for 5 h at different temperatures.

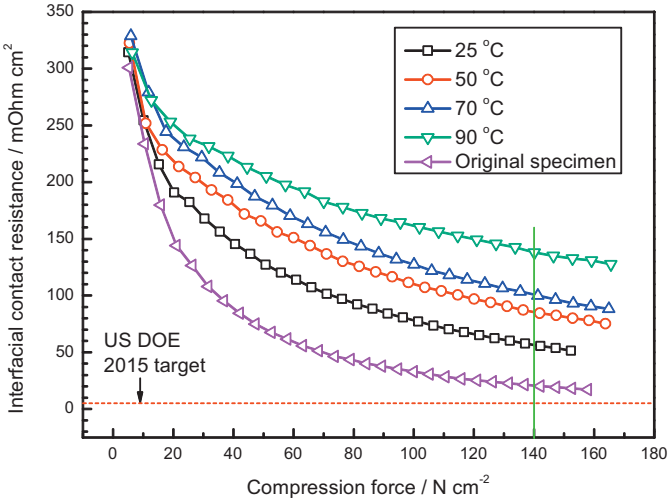

Fig. 9. ICR between carbon paper and SS316L polarized for 5 h at different temperature in 1×10^{-5} M $H_2SO_4 + 6 \times 10^{-4}$ M F^- solution compared with that of the original specimen.

4. Conclusions

The effect of temperature on the corrosion behavior of SS316L in simulated PEMFC cathode environments is systematically studied through potentiodynamic polarization, potentiostatic measurements, AFM (surface morphology examination), the Mott–Schottky analysis, XPS (composition profiles), and PEC measurements (band gap energy). The following conclusions can be obtained from this study:

- Within the temperature range studied (25–90 °C) SS316L consistently displays the self-passivation behavior in simulated PEMFC cathode environments, and the passive region becomes narrower and the pitting potential decreases with the increase of temperature.
- At a given cell potential, the corrosion behavior of SS316L can be significantly different at different temperatures in PEMFC cathode environments.
- Within the temperature range studied (25–90 °C), after different passivation time, the corrosion current densities of SS316L are all lower than US DOE 2015 target, 1 μA cm^{-2}.
- Though the thickness of the passive film increases with temperature, the equilibrium corrosion current density increases with temperature.
- The passive films are of bi-layer (p–n type) semiconductor, but the p-type semiconductor behavior becomes weaker with the increase of temperature and at high temperature (e.g. 90 °C), the bi-layer structure disappears.
- The passive films are mainly composed of Fe oxide and Cr oxide. The content of Cr oxide and thus the bad gap energy decrease with temperature, leading to accelerated corrosion.
- The interfacial contact resistance between carbon paper and polarized SS316L does not satisfy the US DOE 2015 target and it increases with the environment temperature.

Acknowledgements

The financial supports from Chang Jiang Scholars Program of Ministry of Education of China, the National Science Foundation of China (No. 50821064) and National Basic Research Program of China (No. 2009CB220000) are gratefully acknowledged. The authors would also like to thank Ms. Penghui Guo for her assistance in the XPS measurements.

References

[1] G. Hoogers, in: G. Hoogers (Ed.), Fuel Cell Technology Handbook, CRC Press LLC, Boca Raton, 2003, pp. 1–5.
[2] J. Larminie, A. Dicks, Fuel Cell Systems Explained, John Wiley & Sons Ltd., West Sussex, 2003.
[3] Y. Wang, D.O. Northwood, Electrochim. Acta 52 (2007) 6793–6798.
[4] A. Agneaux, M.H. Plouzennec, L. Antoni, J. Granier, Fuel Cells 6 (2006) 47–53.
[5] H. Wang, M.A. Sweikart, J.A. Turner, J. Power Sources 115 (2003) 243–251.
[6] V.V. Nikam, R.G. Reddy, S.R. Collins, P.C. Williams, G.H. Schiroky, G.W. Henrich, Electrochim. Acta 53 (2008) 2743–2750.
[7] A. Pozio, F. Zaza, A. Masci, R.F. Silva, J. Power Sources 179 (2008) 631–639.
[8] A.M. Lafront, E. Ghali, A.T. Morales, Electrochim. Acta 52 (2007) 5076–5085.
[9] L. Ma, S. Warthesen, D.A. Shores, J. New Mater. Electrochem. Syst. 3 (2000) 221–228.
[10] Y. Wang, D.O. Northwood, J. Power Sources 163 (2006) 500–508.
[11] R.L. Borup, N.E. Vanderborgh, Mater. Res. Soc. Symp. Proc. 393 (1995) 151.
[12] K.S. Weil, G. Xia, Z.G. Yang, J. Yong Kim, Int. J. Hydrogen Energy 32 (2007) 3724–3733.
[13] W. Yoon, X. Huang, P. Fazzino, K.L. Reifsnider, M.A. Akkaoui, J. Power Sources 179 (2008) 265–273.
[14] M. Wilkinson, M. Blanco, E. Gu, J.J. Martin, D.P. Wilkinson, J.J. Zhang, H. Wang, Electrochem. Solid State Lett. 9 (2006) A507–A511.
[15] C.-Y. Wen, G.-W. Huang, J. Power Sources 178 (2008) 132–140.
[16] B. Sørensen, Hydrogen and Fuel Cells: Emerging Technologies and Applications, Elsevier Academic Press, Burlington, 2005.
[17] T. Fabian, R. O'Hayre, F.B. Prinz, J.G. Santiago, J. Electrochem. Soc. 154 (2007) B910–B918.
[18] V.V. Nikam, R.G. Reddy, J. Power Sources 152 (2005) 146–155.
[19] S. Jin, E. Ghali, A.T. Morales, J. Power Sources 162 (2006) 294–301.
[20] K.M. El-Khatib, M.O.A. Helal, A.A. El-Moneim, H. Tawfik, Anti-Corros. Method Mater. 51 (2004) 136.
[21] M.A.L. Garcia, M.A. Smit, J. Power Sources 158 (2006) 397–402.
[22] R.F. Silva, D. Franchi, A. Leone, L. Pilloni, A. Masci, A. Pozio, Electrochim. Acta 51 (2006) 3592–3598.
[23] Y. Yang, L. Guo, H. Liu, J. Power Sources 195 (2010) 5651–5659.
[24] Y. Yang, L. Guo, H. Liu, Int. J. Hydrogen Energy 36 (2011) 1654–1663.
[25] D.T. Sawyer, A. Sobkowiak, J.L. Roberts Jr., Electrochemistry for Chemists, John Wiley & Sons, Inc., New York, 1995.
[26] C.G. Zoski, Handbook of Electrochemistry, Elsevier, Oxford, 2007.
[27] P.H. Rieger, Electrochemistry, Chapman & Hill, Inc., New York, 1994.
[28] R.M. Carranza, M.G. Alvarez, Corros. Sci. 38 (1996) 909–925.
[29] T.L.S.L. Wijesinghe, D.J. Blackwood, Appl. Surf. Sci. 253 (2006) 1006–1009.
[30] A. Fattah-alhosseini, A. Saatchi, M.A. Golozar, K. Raeissi, Electrochim. Acta 54 (2009) 3645–3650.
[31] U. S. Department of Energy, Multi-year research, development and demonstration plan: planned program activities for 2005–2015, 2007, http://www1.eere.energy.gov/hydrogenandfuelcells/mypp/pdfs/fuel_cells.pdf, pp. 3.4–26.
[32] M.D. Archer, A.J. Nozik, Nanostructured and Photoelectrochemical Systems for Solar Photon Convertion, Imperial College Press, London, 2003.
[33] R. De Gryse, W.P. Gomes, F. Cardon, J. Vennik, J. Electrochem. Soc. 122 (1975) 711–712.
[34] M.G.S. Ferreira, M.D.C. Belo, N.E. Hakiki, G. Goodlet, M.F. Montemor, A.M.P. Simões, J. Br. Chem. Soc. 13 (2002) 433–440.
[35] M.F. Montemor, M.G.S. Ferreira, N.E. Hakiki, M.D. Belo, Corros. Sci. 42 (2000) 1635–1650.
[36] W.W. Gärtner, Phys. Rev. 116 (1959) 84.
[37] G. Goodlet, S. Faty, S. Cardoso, P.P. Freitas, A.M.P. Simões, M.G.S. Ferreira, M. Da Cunha Belo, Corros. Sci. 46 (2004) 1479–1499.
[38] S. Piazza, M. Sperandeo, C. Sunseri, F. Di Quarto, Corros. Sci. 46 (2004) 831–851.